Table S1. CMIP6 climate model simulations examined in this study. The spatial resolution of each model output is given as the number of grid points (longitude × latitude).

No.	Model	Institution & Nation	Lon × Lat	Realization
1	ACCESS-CM2	Commonwealth Scientific and Industrial Research Organisation (CSIRO)-Australian Research Council Centre of Excellence for Climate System Science (ARCCSS), Australia	192 × 144	r1i1p1f1
2	ACCESS-ESM1-5		192 × 145	r1i1p1f1
3	BCC-CSM2-MR	Beijing Climate Center(BCC), China	320 ×160	r1i1p1f1
4	BCC-ESM1		128 × 64	r1i1p1f1
5	CanESM5	Canadian Centre for Climate Modelling and Analysis (CCCma), Canada	128 × 64	r1i1p1f1
6	CESM2	National Center for Atmospheric Research (NCAR), USA	288 × 192	r1i1p1f1
7	CESM2-WACCM		288 × 192	r1i1p1f1
8	CESM2-WACCM-FV2		144 × 96	r1i1p1f1
9	CNRM-CM6-1	Centre National de Recherches Meteorologiques-Centre Europeen de Recherche et de Formation Avancee en Calcul Scientifique (CNRM-CERFACS), France	256 × 128	r1i1p1f2
10	CNRM-CM6-1-HR		720 × 360	r1i1p1f2
11	CNRM-ESM2-1		256 × 128	r1i1p1f2
12	EC-Earth3	EC-Earth-Consortium, European countries	512 × 256	r1i1p1f1
13	EC-Earth3-Veg		512 × 256	r1i1p1f1
14	FGOALS-g3	Chinese Academy of Sciences (CAS), China	180 × 80	r1i1p1f1
15	GFDL-CM4	National Oceanic and Atmospheric Administration Geophysical Fluid Dynamics Laboratory (NOAA-GFDL), USA	144 × 90	r1i1p1f1
16	INM-CM5-0	Centre for Climate Change Research, Indian Institute of Tropical Meteorology Pune (CCCR-IITM), India Institute for Numerical Mathematics (INM), Russia	180 × 120	r1i1p1f1
17	IPSL-CM6A-LR	Institut Pierre Simon Laplace (IPSL), France	144 × 143	r1i1p1f1
18	MIROC6	Japan Agency for Marine-Earth Science (JAMSTEC), Atmosphere and Ocean Research Institute (AORI), National Institute for Environmental Studies (NIES), and RIKEN Center for Computational Science (R-CCS), Japan	256 × 128	r1i1p1f1
19	MIROC-ES2L		128 × 64	r1i1p1f1
20	MPI-ESM-1-2-HAM	Max Planck Institut fur Meteorologie (MPI), Germany	192 × 96	r1i1p1f1
21	MPI-ESM1-2-HR		384 × 192	r1i1p1f1
22	MPI-ESM1-2-LR		192 × 96	r1i1p1f1
23	MRI-ESM2-0	Meteorological Research Institute	192 × 96	r1i1p1f1

No.	Model	Institution & Nation	Lon × Lat	Realization
		(MRI), Japan		
24	NESM3	Nanjing University of Information Science and Technology (NUIST), China	192 × 96	r1i1p1f1
25	SAM0-UNICON	Seoul National University(SNU), Korea	288 × 192	r1i1p1f1
26	TaiESM1	Research Center for Environmental Changes (AS-RCEC), Taiwan	288 × 192	r1i1p1f1
27	UKESM1-0-LL	National Environmental Research Council(NERC), UK	192 × 144	r1i1p1f2

Table S2. List of ESSPV and EWSPV winters. Years highlighted in red (blue) denote WQBO (EQBO) winters.

ESSPV winters	**EWSPV winters**
1982/83, 1989/90, 1991/92, 1992/93, 1993/94, 1994/95, 1995/96, 1997/98, 1999/2000, 2002/03, 2013/14, 2019/20, 2021/22	**1984/85, 1986/87, 1987/88, 1998/99, 2000/01, 2003/04, 2005/06, 2008/09, 2009/10, 2012/13, 2017/18, 2018/19, 2020/21**

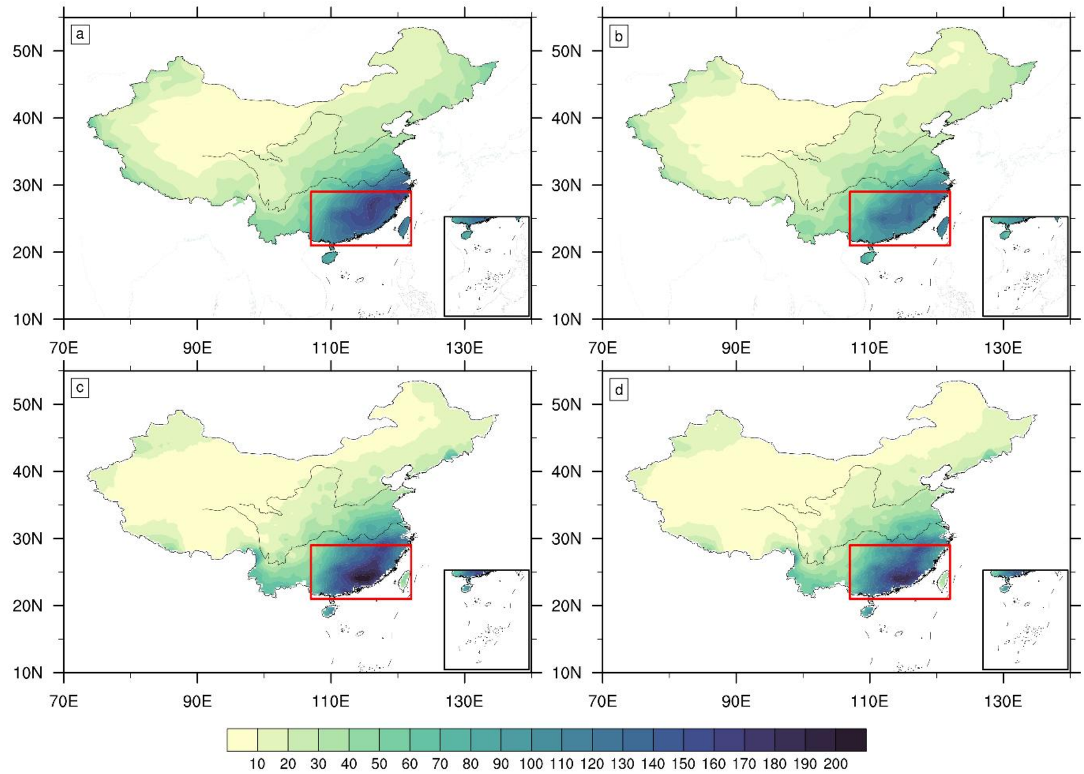

Figure S1. Standard deviation of winter total precipitation and extreme precipitation over China. (a) Standard deviation of NDJFM total precipitation (unit: mm) over China from the GPCP dataset. **(b)** Same as **(a)**, but for extreme precipitation (R90). **(c, d)** Same as **(a, b)**, but using the CN05.1 dataset.

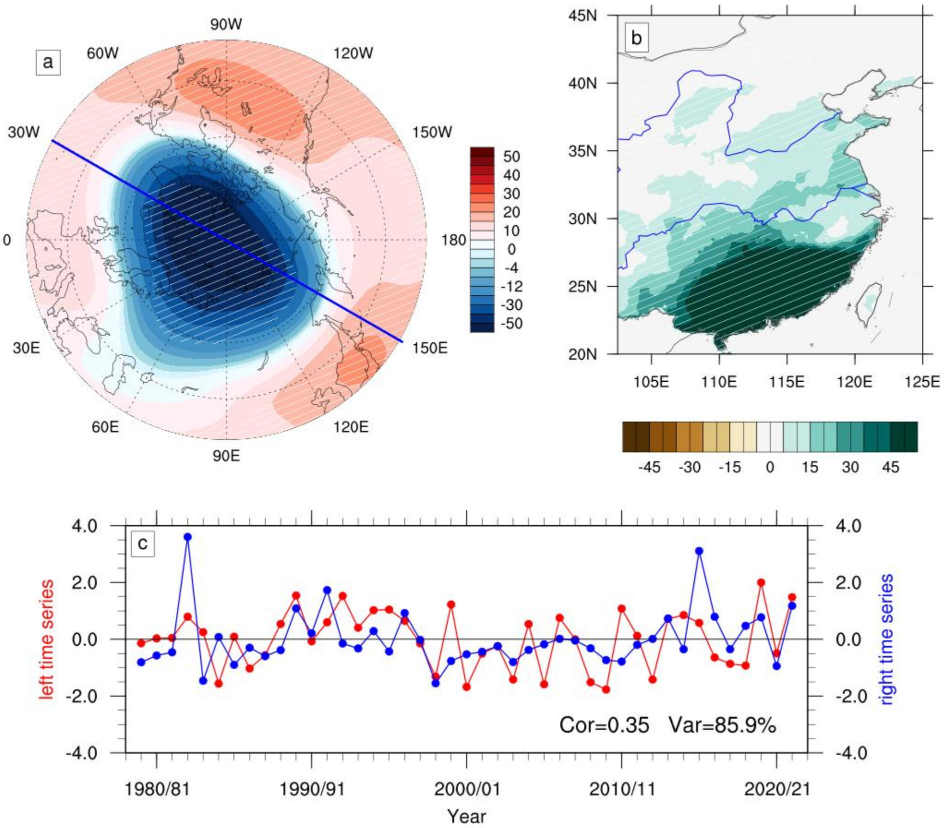

Figure S2. SVD patterns of 50-hPa geopotential height and extreme precipitation over eastern China. (a, b) Homogeneous correlation patterns of the first SVD mode between **(a)** NDJFM-mean 50-hPa geopotential height anomalies north of 30°N (left field) (unit: gpm) and **(b)** NDJFM-mean R90 anomalies over eastern China (20°–40°N, 105°–125°E; right field) (unit: mm). **(c)** Time series of the expansion coefficients for the left and right fields. The temporal correlation between the two expansion coefficients is 0.35, and this mode accounts for 85.9% of the total squared covariance.

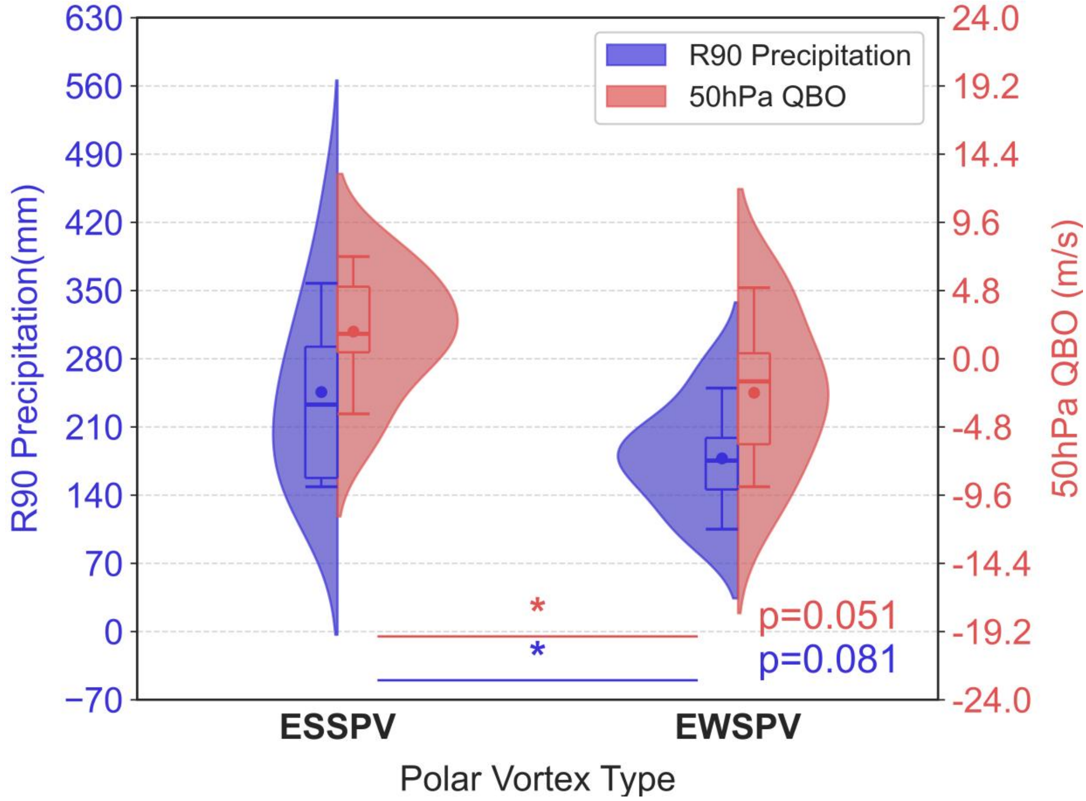

Figure S3. Vertical cross-section of zonal wind under different SPV regimes. Pressure–latitude cross section of the composite difference in zonal wind anomaly (shading, unit: m s^{-1}) averaged over 30°W–150°E between ESSPV and EWSPV winters.

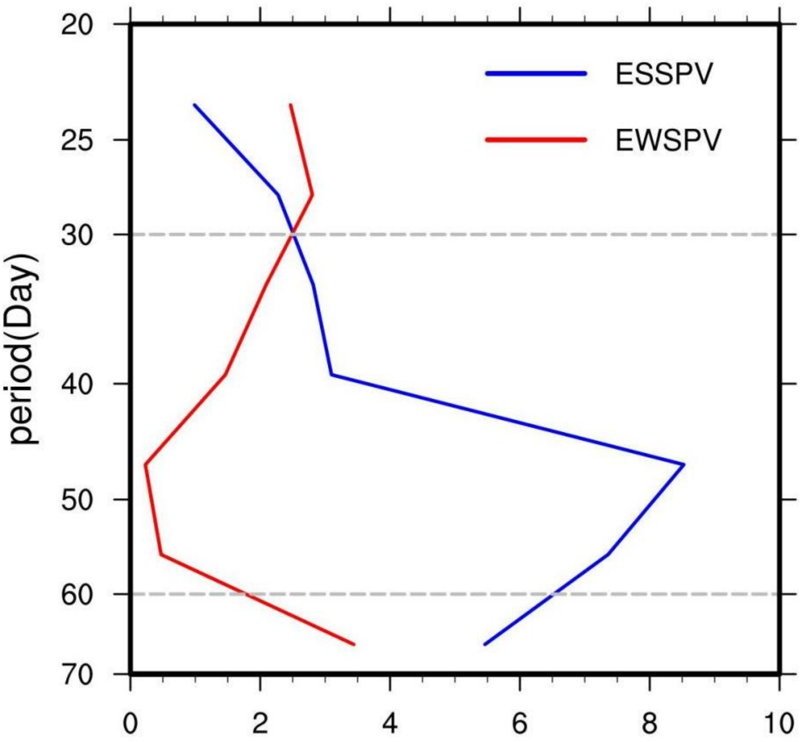

Figure S4. Precipitation variability under SPV modulation. Mean power spectra of regionally averaged daily precipitation anomalies over SC (purple box in Fig. 1g) during NDJFM for each ESSPV (blue) and EWSPV (red) winter.

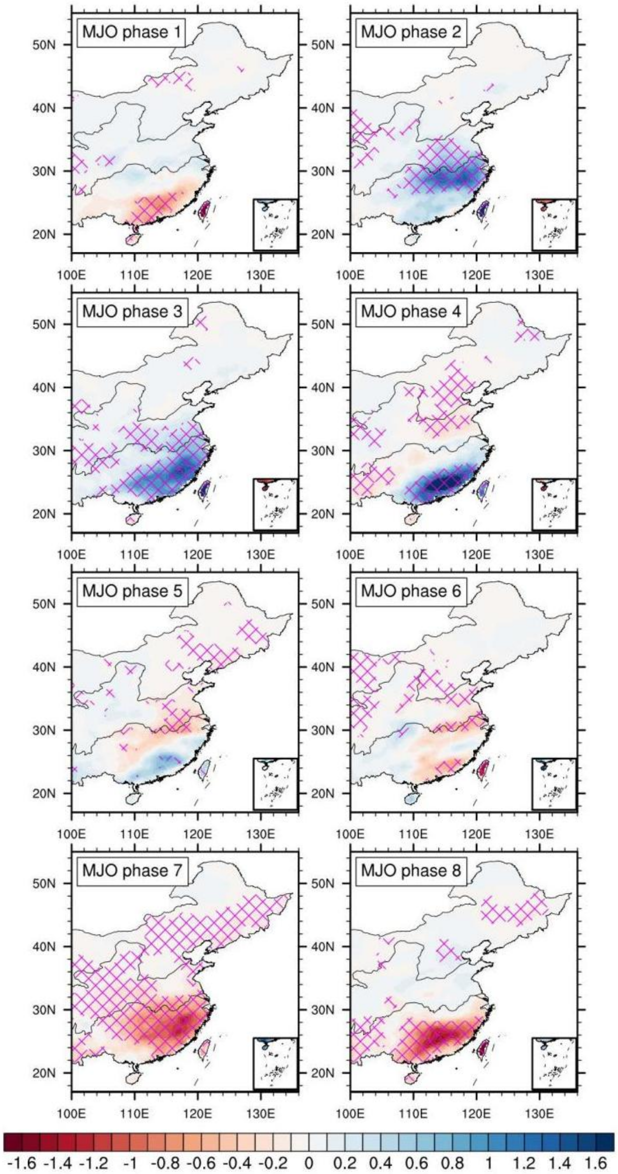

Figure S5. MJO impacts on precipitation over eastern China. Composite evolution patterns of MJO phases 1–8 precipitation anomalies (unit: mm day^{-1}) during NDJFM. Meshes indicate significant precipitation anomalies at the 95% confidence level.

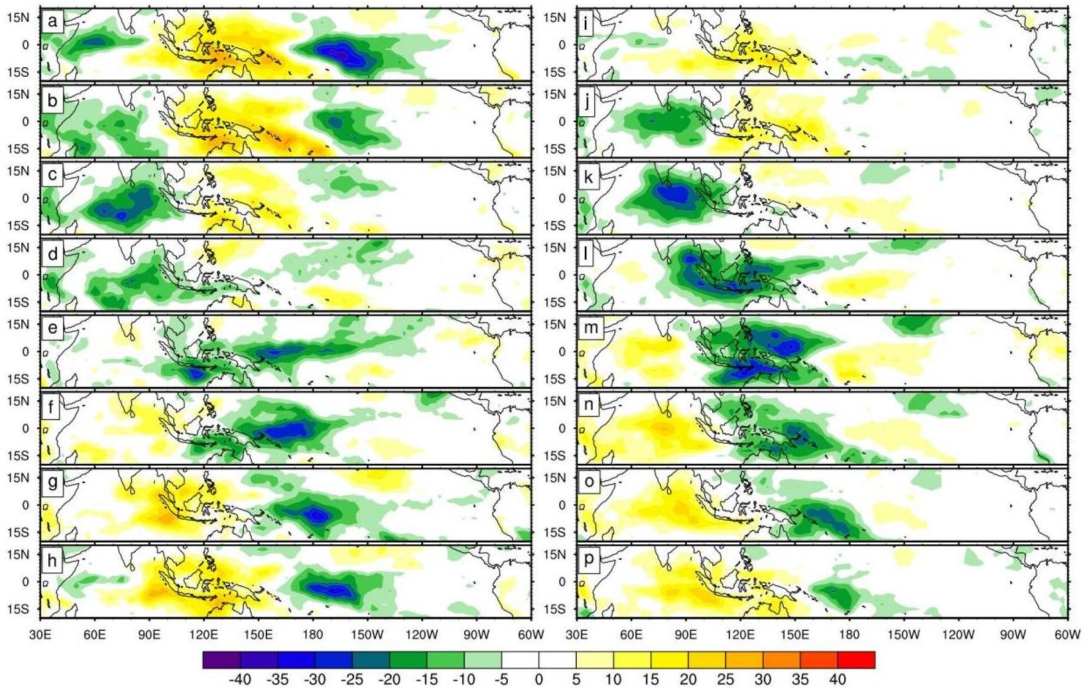

Figure S6. Evolution of MJO convection under different SPV backgrounds. Composites of OLR anomalies (green–yellow shading; W m^{-2}) for MJO phases 1–8 under **(a–h)** ESSPV winters and **(i–p)** EWSPV winters.

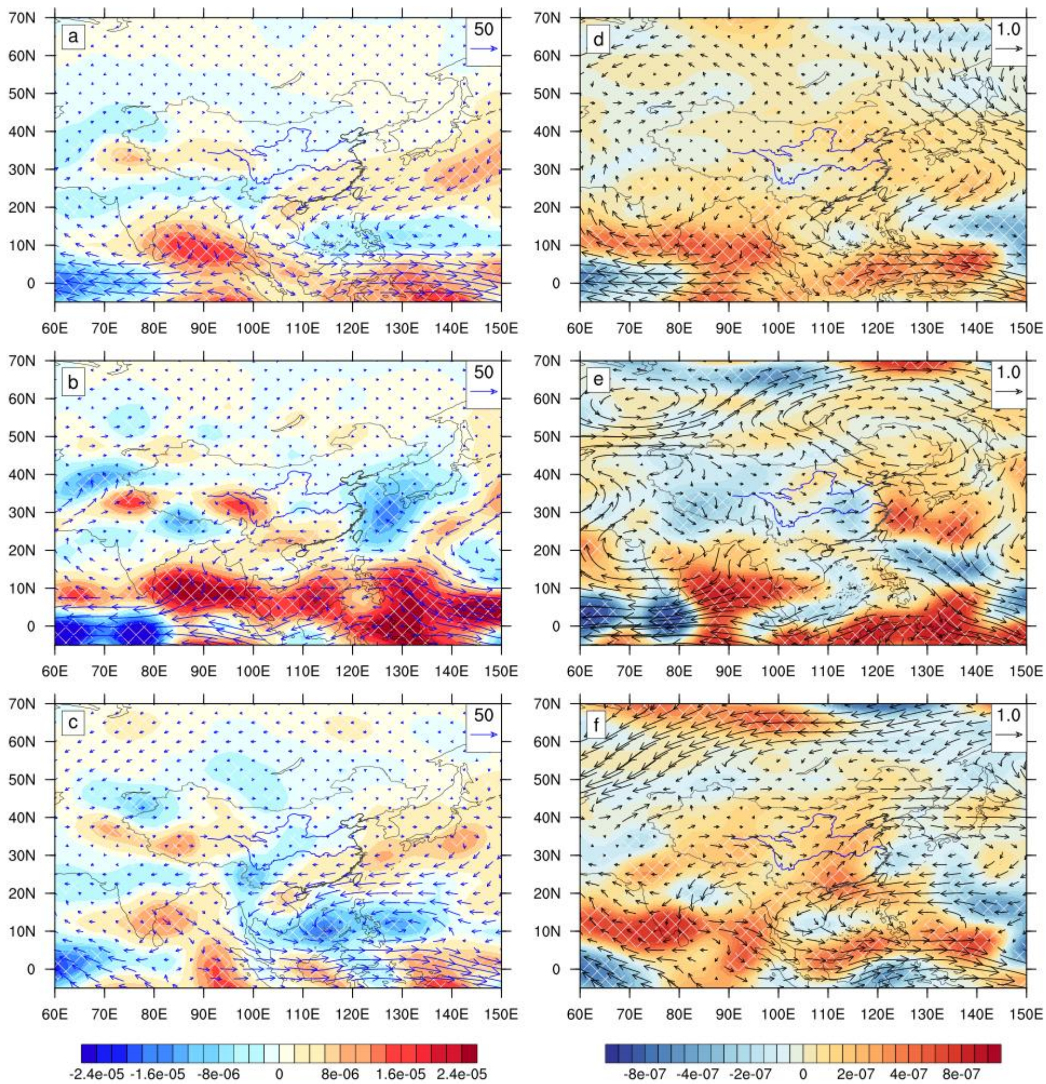

Figure S7. Circulation responses under the synergistic impacts of ESSPV and MJO phases 6–8 and 1. (a–c) Composites of vertically integrated (surface to 300 hPa) water vapor fluxes (vectors, unit: kg m^{-1} s^{-1}) and their divergence (shading, unit: kg m^{-2} s^{-1}) during MJO phases 6–8 and 1 for **(a)** all winters, **(b)** ESSPV winters, and **(c)** EWSPV winters. **(d–f)** Same as **(a–c)**, but for 850-hPa horizontal winds (vectors, unit: m s^{-1}) and their divergence (shading, unit: s^{-1}). Meshes indicate significant anomalies at the 95% confidence level.

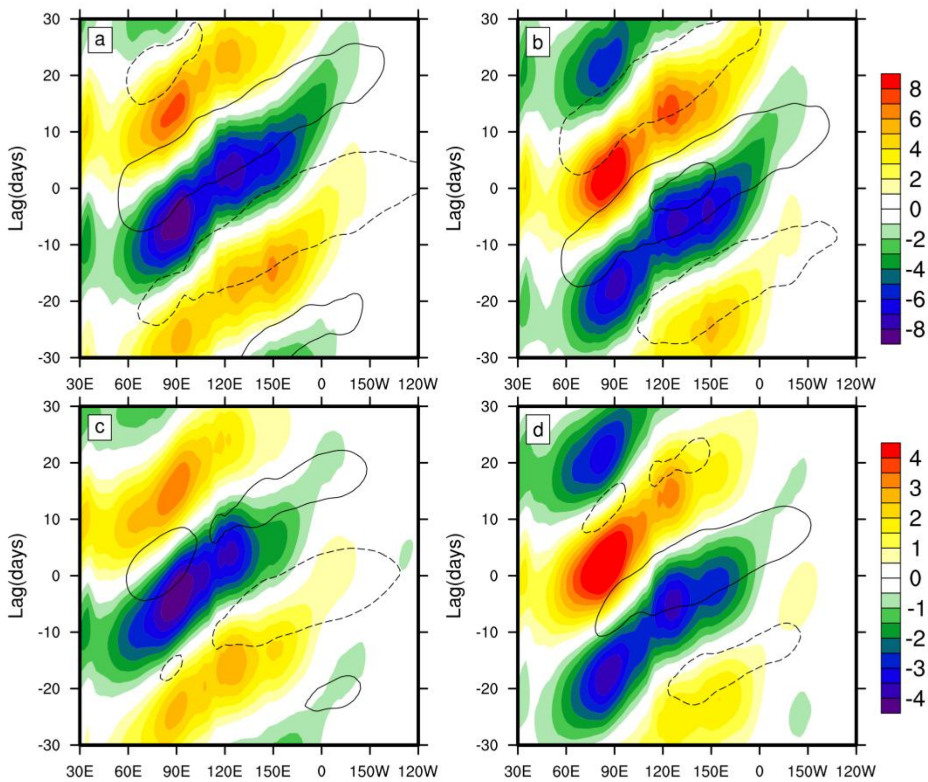

Figure S8. Hovmöller diagrams of the MJO derived from observations and CMIP6 models. (a) Longitude–time cross section of the 30–60-day bandpass-filtered MJO PC1 index regressed OLR anomaly (green–yellow shading, unit: W m^{-2}) and 850-hPa zonal wind anomaly (contours, interval of 0.5 m s^{-1}; zero contours are omitted) averaged over 15°S–15°N from 30-day lead to 30-day lag during winter. **(b)** Same as **(a)**,but for the MJO PC2 index. **(c–d)** Same as **(a–b)**, but for the multi-model mean of all CMIP6 models.

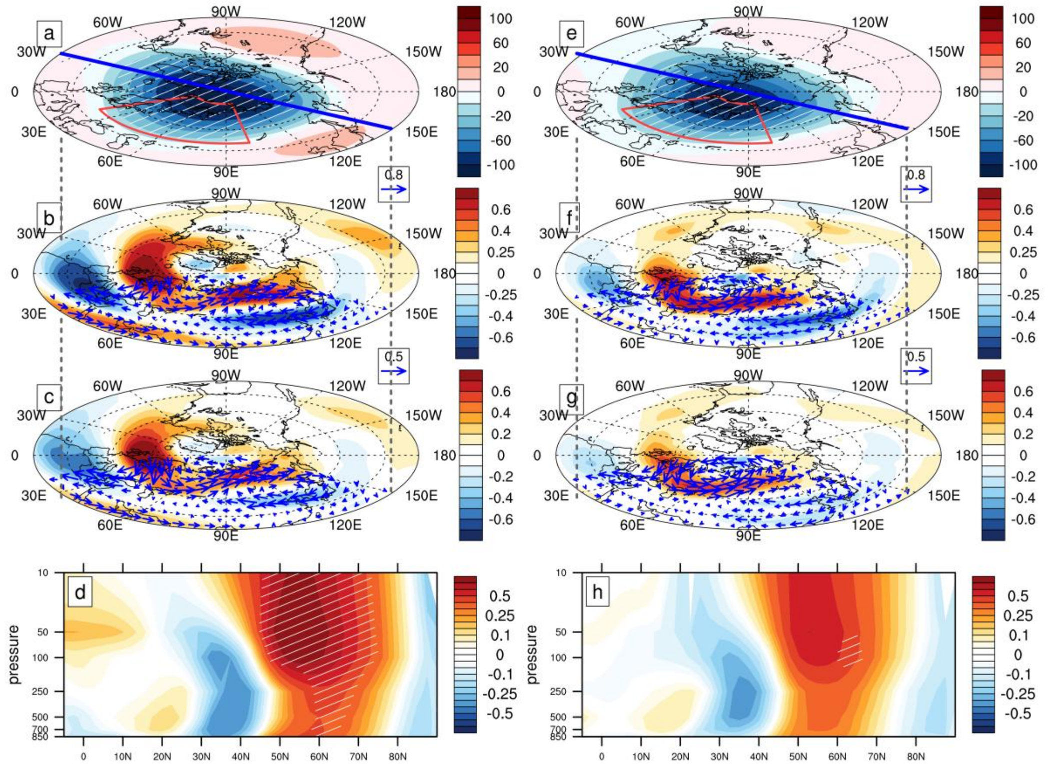

Figure S9. Circulation background and responses of extreme precipitation over SC under SPV modulation for SPV-MME1 and SPV-MME2. (a) Regressed NDJFM mean 50-hPa geopotential height anomalies (shading, unit: gpm) and correlation coefficients (green dashed contours; interval −0.05, starting from −0.1) onto the regionally averaged R90 anomaly over SC for SPV-MME1. White slashes indicate regressed geopotential height anomalies significant at the 95% confidence level. **(b)** Regressed NDJFM mean 500-hPa horizontal wind anomalies (vectors, unit: m s^{-1}, only those significant at the 95% confidence level are shown) and the zonal wind component (shading, unit: m s^{-1}) onto the ESSPV index (multiplied by −1) for SPV-MME1. White slashes indicate significant zonal wind anomalies at the 95% confidence level. **(c)** Same as **(b)**, but for 700-hPa horizontal wind anomalies (vectors, unit: m s^{-1}, only those significant at the 95% confidence level are shown) and the zonal wind component (shading, unit: m s^{-1}). **(d)** Pressure–latitude cross section of correlation coefficients between the zonal wind anomalies averaged over 30°W–150°E and the ESSPV index for SPV-MME1. White slashes indicate significant correlation coefficients at the 95% confidence level. **(e–h)** Same as **(a–d)**, but for SPV-MME2.